

Strain-Induced Lateral Heterostructures in Patterned Semiconductor Nanomembranes for Micro- and Optoelectronics

Abdullah Gok,* Xiaowei Wang, Shelley Scott, Abhishek Bhat, Hanfei Yan, Ajith Pattammattel, Evgeny Nazaretski, Yong S. Chu, Zicong Huang, Richard M. Osgood, Jr, Max G. Lagally, and Roberto Paiella*



Cite This: *ACS Appl. Nano Mater.* 2021, 4, 6160–6169



Read Online

ACCESS |



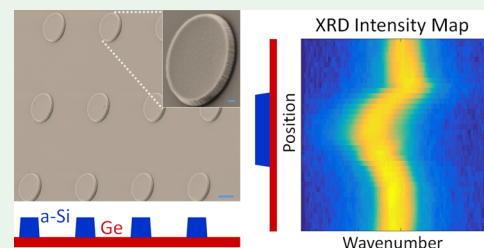
Metrics & More



Article Recommendations

ABSTRACT: The ability to tailor the energy band lineup of semiconductor materials plays a key role in the development of many electronic and optoelectronic devices and normally relies on heteroepitaxy. Here, we report a different method, based on strain engineering, for the controlled introduction of variations in bandgap energy with lateral position in thin films. External stress is applied on Ge nanomembranes stacked with an array of amorphous-Si pillars in order to create a non-uniform strain (and therefore bandgap energy) distribution commensurate with the sample thickness variations. The resulting strain profiles are mapped using Bragg diffraction with a hard X-ray probe featuring nanoscale spatial resolution. Compared with traditional heterostructures grown by epitaxial techniques, these strain-engineered samples involve a single chemical composition and are not limited in the choice of compatible materials by any restriction imposed by lattice-matching requirements. Furthermore, their energy band lineups can be patterned in nearly arbitrary shapes using nanolithography to control the thickness profile and can be tuned actively by varying the applied stress. As a result, these structures are attractive for a wide range of device applications (including lasers, LEDs, solar cells, and thermoelectrics) that require complex heterostructure lineups with multiple bandgap energies.

KEYWORDS: strain engineering, semiconductor nanomembranes, nanofabrication patterning, X-ray nanodiffraction imaging, energy band lineups



INTRODUCTION

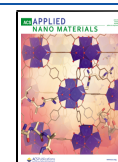
Semiconductor heterostructures with tailored energy band profiles are used in countless electronic and optoelectronic devices (from transistors to lasers, LEDs, and photodetectors) and, in fact, historically, they have often enabled dramatic advances in device performance and even created new functionalities.^{1,2} A particularly significant example can be found in the development of semiconductor lasers, where room-temperature operation could only be achieved after the introduction of double-heterojunction active layers.³ Traditionally, these composite materials are synthesized by heteroepitaxy, where films of different compositions are grown on top of one another through various atomic deposition techniques, such as molecular-beam and vapor-phase epitaxy. Three-dimensional heterostructures, in which composition varies as a function of in-plane position as well as along the growth direction, can also be constructed with a combination of lithographic surface patterning and heteroepitaxial regrowth, or, in specific materials systems, via strain-driven spontaneous self-assembly. These techniques are well-established in micro- and optoelectronics, where they provide a powerful tool to shape the energy band profile as a way to promote and enhance desired device functionalities.

In addition to varying the chemical compositions, the band structure of a crystalline solid can also be controlled through the judicious introduction of strain. For example, in typical group IV and III–V semiconductors, in-plane biaxial tensile strain has the effect of decreasing the fundamental energy bandgap, while at the same time lifting the degeneracy of the heavy-hole and light-hole valence-band maxima [Figure 1a,b].⁴ Once again, heteroepitaxy provides the standard technique for engineering strain in semiconductors, through the pseudomorphic growth of sufficiently thin films on lattice-mismatched substrates. Under these conditions, a uniform biaxial strain distribution is introduced across the film volume, which can also be employed for various device applications, e.g., to increase speed in transistors⁵ or decrease the transparency threshold in diode lasers.⁶ More recently, the development of

Received: April 8, 2021

Accepted: May 28, 2021

Published: June 10, 2021



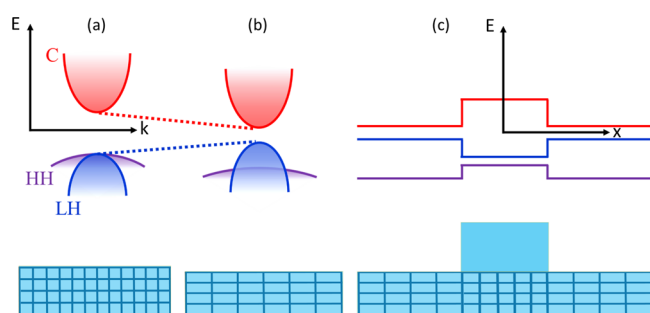


Figure 1. Bandgap engineering by strain. (a,b) Schematic energy band structure (electronic energy E vs crystal wavevector k) of a typical group IV or III–V semiconductor material in its unstrained form (a) and in the presence of biaxial tensile strain (b), showing the conduction (C) band and the heavy-hole (HH) and light-hole (LH) valence bands. (c) Energy band lineup (band-edge energy E vs position x) of a tensilely strained film of the same material, where the center region is coated with an overlying pillar, causing a reduction in the local strain. A schematic cross-sectional view of the semiconductor crystal is shown at the bottom of each panel.

high-quality crystalline nanomaterials has enabled entirely new opportunities for strain engineering, including the external application of mechanical stress in nanowires^{7–10} and nanomembranes (NMs),^{11–15} and the deposition and partial release of suitable stressor layers on patterned micro- and nanostructures.^{16–19} The key idea in this respect is that strain energy increases proportionally to volume and, when it exceeds the thermodynamic and kinetic barriers for strain relief, plastic relaxation occurs.²⁰ Therefore, in the presence of external stress, the smaller the sample cross-sectional area (as in a nanowire or NM), the larger the maximum achievable strain before the onset of plastic deformation. For similar reasons, if the cross-sectional area varies with position along the direction of the applied stress, a non-uniform strain (and therefore bandgap) distribution is produced, with the largest strain accumulating in the thinnest regions and vice versa [Figure 1c].

These considerations suggest a novel approach for the development of crystalline samples featuring controlled spatial variations in bandgap energy. In the present work, this approach is investigated using semiconductor NMs, i.e., single-

crystal sheets with macroscale lateral dimensions and thicknesses smaller than 1 μm that are fully released from their native substrates. By virtue of their extreme geometrical aspect ratios, these nanostructures can provide a degree of mechanical flexibility similar to that of soft polymeric materials,²¹ which makes them generally attractive for basic studies and device applications of strain engineering and flexible (opto)electronics.^{22,23} Specifically, we employ Ge NMs patterned with amorphous-Si (a-Si) pillars [Figure 2a,b] and subjected to isotropic in-plane expansion introduced with a gas pressure cell [Figure 2c]. With this arrangement, a smaller tensile strain can be expected in the NM regions directly underneath the pillars, where the overall sample thickness is larger, relative to the thinner regions in between neighboring pillars. The use of a pillar material with relatively high stiffness, such as a-Si, is also beneficial to promote this effect. Because the bandgap energy decreases with increasing tensile strain as discussed above [Figure 1c], the end result is a controlled bandgap modulation—i.e., the formation of a sample that effectively behaves like a lateral (in-plane) heterostructure but consisting of a single semiconductor material with uniform chemical composition.²⁴ The resulting strain distribution in the NM lattice is measured with the hard-X-ray nanoprobe (HXN) beamline of the National Synchrotron Light Source II (NSLS-II) at Brookhaven National Laboratory. Relative to other techniques for strain measurement, such as Raman microscopy and standard X-ray diffraction (XRD), this system offers a unique combination of ultrahigh spatial resolution, large signal-to-noise ratio, high sensitivity to relative strain variations, and wide-range scanning capabilities,^{25–28} as needed to fully resolve the lateral strain profile in our patterned NM samples.

Compared with traditional heteroepitaxial systems, the strain-induced heterostructures reported in this work feature a number of distinctive properties and capabilities. First, they do not suffer from any restrictions imposed by lattice-matching requirements, which in contrast severely limit the choice of material compositions and thicknesses that can be grown epitaxially on top of one another without plastic deformation. Second, their bandgap spatial variations can be patterned in nearly arbitrary shapes by controlling the sample thickness profile with standard nanolithography techniques. Furthermore, their energy band offsets (proportional to the strain

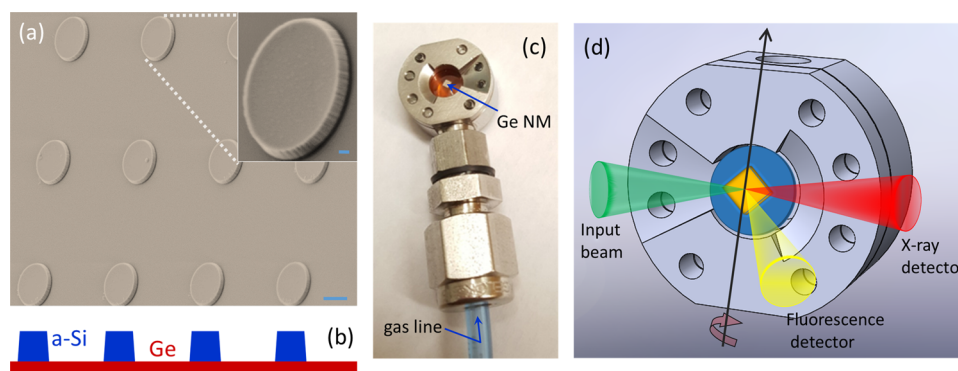


Figure 2. Experimental samples and measurement setup. (a) SEM image of a Ge NM coated with a periodic array of a-Si pillars, with a close-up view of a single pillar in the inset. The scale bar is 2 μm in the main image and 300 nm in the inset. (b) Schematic cross section showing a set of a-Si pillars (blue regions) on a Ge NM (red rectangle) (not drawn to scale). (c) Photograph of the pressure cell loaded with a Ge NM on a polyimide film. The diameter of the sample mount is 14 mm. (d) Schematic illustration of the experimental geometry, showing the direction of the incident and diffracted X-ray beams and the collection angle of the fluorescence detector, relative to the plane of a NM (shown in yellow) mounted on the pressure cell. In the XRD measurements, the sample mount is rotated around the direction shown by the black arrow.

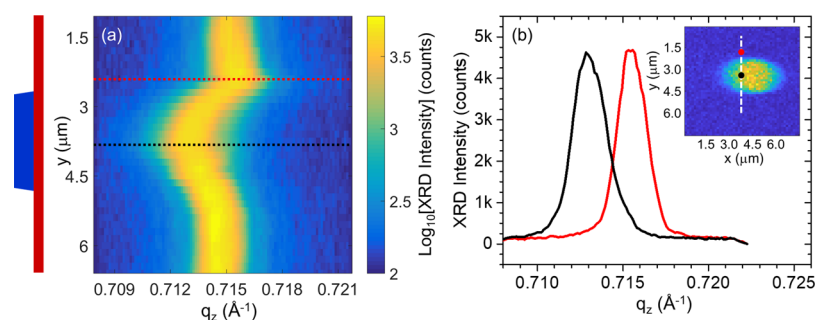


Figure 3. XRD measurement results. (a) Intensity of the (004) Bragg reflection peak of sample A at an applied gas pressure of 414 kPa, plotted as a function of out-of-plane wavenumber q_z for different positions y on the NM plane. The step scan size along the y direction in these measurements is 200 nm. The schematic cross-sectional image on the left-hand side of the plot illustrates the position and width of the overlying a-Si pillar (blue region) on the Ge NMs (red region). (b) Line profiles along the dashed lines of panel (a). Inset: X-ray fluorescence intensity map for the Si K α emission line recorded simultaneously with the same sample at the same pressure. The dashed-line indicates the positions at which the data of panel (a) were measured. The red and black traces of the main plot correspond to the positions denoted by the red and black dots, respectively.

difference between the thick and thin NM regions) can be tuned actively by varying the applied mechanical stress. The combination of these features is also attractive relative to prior work on the controlled introduction of inhomogeneous strain profiles in semiconductors.^{29–31} These previous activities have focused on the deposition of nanoscale stressors on rigid GaAs quantum-well samples,²⁹ the self-organized epitaxial growth of Ge nanoislands on free-standing Si nanoribbons to produce a one-dimensional periodic strain modulation,³⁰ and the release of suspended Ge nanowires of non-uniform width in a Ge-on-insulator (GOI) substrate to concentrate the pre-existing tensile strain in the narrower regions along the wire axis.³¹ Compared to these techniques, the present approach offers significantly enhanced design flexibility to control the strain-induced energy band lineup, both geometrically through the shape and distribution of the pillar array and actively through the externally applied gas pressure. Additionally, because of the NM extended planar geometry, this approach allows for two-dimensional bandgap patterning and is intrinsically scalable to large device areas with no constraints on the lateral dimensions. Future device applications that can be expected to benefit from these capabilities include multiple-junction solar cells, superlattice thermoelectric generators, and broadband white LEDs, where the use of such strain-induced lateral heterostructures may enable further advances in bandgap engineering, as well as enhanced functionality (e.g., dynamic reconfigurability) and extension to novel materials systems.

RESULTS AND DISCUSSION

The samples used in these experiments consist of 90 nm-thick (001) Ge NMs released from a commercial GOI substrate by dissolving the underlying buried oxide layer with a selective wet etch in hydrofluoric (HF) acid and then transferred and bonded on a flexible film of polyimide (PI) by a wet transfer process (see [Methods](#) Section).¹² Similar NMs can be fabricated in a wide range of other materials systems, as long as a substrate can be prepared where a thin single-crystal film of the desired NM material initially exists on a suitable sacrificial layer.^{22,23} The formation of strain-induced lateral heterostructures reported in this work can therefore be similarly extended to many other semiconductor materials. At the same time, it should be noted that strain engineering plays a particularly important role in Ge, where, at sufficiently large tensile strain (>1.9% biaxial), the very nature of the fundamental energy bandgap changes from indirect to direct.¹³

As a result, the controlled introduction of tensile strain in Ge provides an effective means to enhance the light emission efficiency^{12,13,16,17,19} and can even enable laser development as shown in recent work.^{32,33} In fact, numerical simulations of (one-dimensional) strain-induced Ge superlattices have suggested that particularly strong direct-bandgap radiative transitions can be achieved in these systems.³⁴

The pillar arrays used to tailor the NM strain profile are fabricated by electron beam lithography with a poly(methyl methacrylate) (PMMA) resist followed by electron beam evaporation of a-Si and liftoff. For simplicity, in the present work, we employ square periodic arrays of cylindrical pillars, although similar strain modulation results can be expected with essentially any arbitrary pillar shape and spatial distribution. In the context of strain-enhanced Ge-NM light-emitting devices, these periodic arrays can also serve as grating out-couplers for in-plane emitted light and photonic crystal cavities.^{35,36} The XRD data presented below were measured with two different samples, one (labeled sample A) with pillar base diameter $D = 1.8\ \mu\text{m}$, pillar height $H = 375\ \text{nm}$, and array periodicity $\Lambda = 5\ \mu\text{m}$ and the other (sample B) with $D = 3.5\ \mu\text{m}$, $H = 300\ \text{nm}$, and $\Lambda = 10\ \mu\text{m}$. As illustrated by the scanning electron microscopy (SEM) image of sample B in [Figure 2a](#), the pillar sidewalls are somewhat sloped due to some accumulation of a-Si on the rims of the patterned PMMA holes during electron beam evaporation, which progressively reduces the hole diameter.

The strain distribution established in these samples under external stress is mapped by monitoring the Ge (004) XRD Bragg reflection peak as a function of in-plane position on the NM. High-resolution XRD provides a very sensitive technique for measuring relative changes in lattice constants and therefore strain in crystalline materials. While standard XRD tools employ relatively large beams (typically a few 100 μm), focused nanoprobe that have recently become available at advanced synchrotron sources can achieve spot sizes smaller than 100 nm.^{25,37} These systems operated in scanning mode combine high angular resolution in reciprocal space with high spatial resolution in real space and therefore are ideally suited to study lateral strain profiles in crystalline samples.^{27,28,38–43} In the present study, these capabilities are particularly significant as a way to enable mapping the strain variations with position on the NM plane around the overlying pillars. At the same time, the determination of absolute strain values with these tools is less accurate without an external calibration

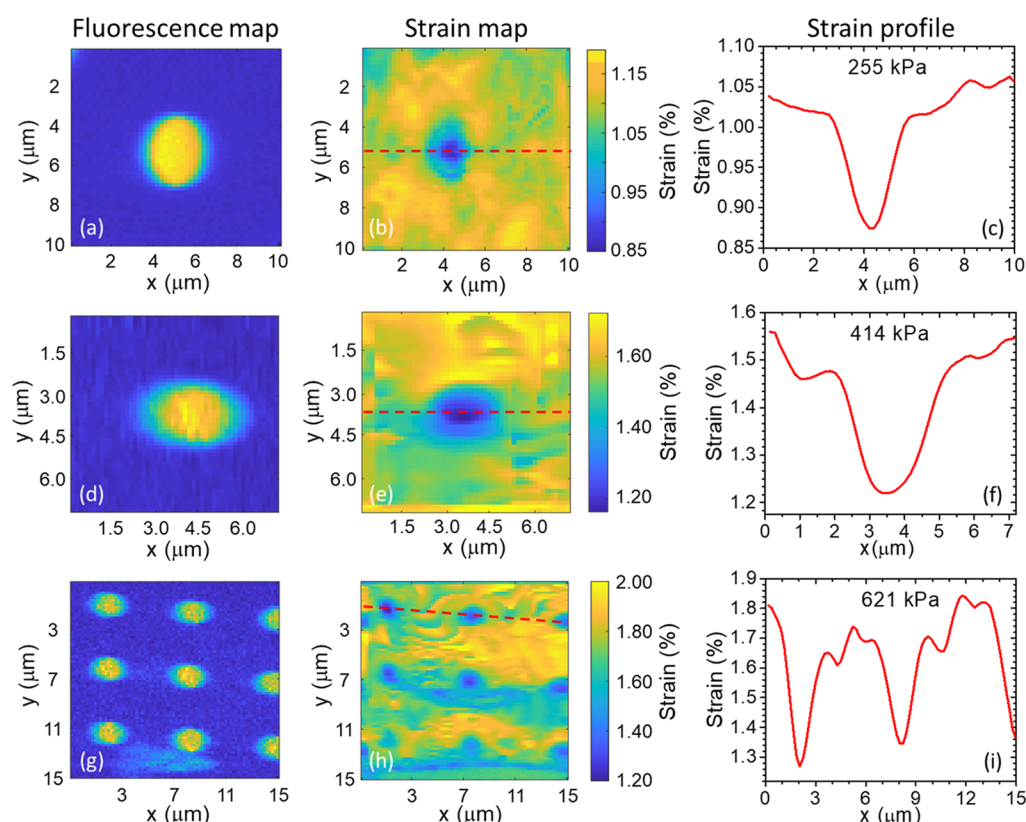


Figure 4. Experimental strain maps. (a–c) Data measured on sample B at a pressure of 255 kPa. (d–f) Data measured on sample A at 414 kPa. (g–i) Data measured on sample A at 621 kPa. Panels (a), (d), and (g) show the X-ray fluorescence intensity maps for the Si $K\alpha$ emission line measured on each sample, indicating the positions and dimensions of the Si pillars. The slightly elongated shapes observed in these plots are a consequence of the spreading of the projected area of the incident beam at oblique angles convoluted with the height of the pillar. The different shape in panel (a) is attributed to geometrical differences between the specific pillar of sample B measured in this map and the pillars of sample A measured in panels (d) and (g). The corresponding in-plane biaxial tensile strain maps are shown in panels (b), (e), and (h). These plots were generated based on the measured Ge (004) XRD patterns, with the results of prior Raman strain measurements on similar Ge NMs without pillars¹² used to calibrate the absolute strain values in the NM regions between the a-Si pillars (see Methods Section). Panels (c), (f), and (i) show the strain profiles along the red dashed lines of (b), (e), and (h), respectively, with a small degree of smoothing (5 point moving average) applied to the experimental data.

reference. Here, we use the findings of prior Raman strain measurements with similar Ge NMs without pillars¹² to calibrate the strain in the NM regions between the a-Si pillars (see Methods Section).

In our experiments, the PI films supporting the NMs are used to seal a circular aperture in a gas pressure cell [Figure 2c,d], which allows for the application of mechanical stress in a highly controllable fashion. When the cell is inflated, the NM effectively sits on the surface of an expanding sphere of PI, with a very large radius of curvature R compared to the NM thickness (90 nm). In particular, simple geometrical considerations based on the diameter of the suspended PI films (5 mm) and the experimental strain levels presented below suggest values of R larger than 8 mm at all measured pressures. As a result, the distortion in the Ge lattice introduced by the applied gas pressure can be assumed to be predominantly isotropic in-plane expansion, with no significant out-of-plane stress due to bending. The pressure cell was designed to comply with the tight geometrical constraints of the XRD nanoprobe sample compartment, which was properly fitted to enable controlling the applied gas pressure *in situ*. The accessible angular range relative to the NM surface inside the pressure cell was sufficiently large to allow for complete measurements of the (004) Bragg reflection peak (except near zero applied pressure, when the NM lies flat within the sample

mount), whereas other diffraction orders of possible interest were partially blocked by the sample mount sidewalls.

The measured XRD data are illustrated in Figure 3a, where we show the intensity of the Ge (004) diffracted beam from sample A at an applied gas pressure of 414 kPa, plotted as a function of out-of-plane wavenumber q_z for different positions y on the NM plane. The different values of y in this plot correspond to different points along the dashed-line in the inset of Figure 3b, which runs across an overlying a-Si pillar (in these experiments, the position and shape of the pillars are determined from the measured fluorescence maps, as discussed below). A significant shift in the center of mass of the diffraction peak is observed as the measured location is moved from the bare NM regions around the pillar to the area immediately below the pillar, indicative of a proportional change in strain. In particular, the XRD signal under the a-Si pillar is peaked at a lower value of q_z compared to the surrounding areas, consistent with a larger out-of-plane Ge lattice constant and hence, by Poisson's ratio, a lower in-plane lattice constant (i.e., a smaller in-plane tensile strain, as expected). This shift is further illustrated in Figure 3b, where we plot the XRD signal intensity as a function of q_z at two representative locations away from and under the pillar. With these measurements, the local strain of each sample can therefore be mapped as a function of position on the NM plane

based on the center of mass of the local diffraction peak (see Methods Section).

The resulting strain maps are presented in Figure 4. Here, the top row [panels (a)–(c)] shows data measured on sample B at an applied gas pressure of 255 kPa. The middle row [panels (d)–(f)] and the bottom row [panels (g)–(i)] correspond to sample A at 414 and 621 kPa, respectively. In all measurements, the pressure inside the XRD sample compartment is about 34 kPa, roughly one-third of the atmospheric pressure. The leftmost plot of each row [Figure 4a,d,g] shows the X-ray fluorescence intensity of the Si $K\alpha$ emission line, mapped across the field of view of each measurement to identify the locations and dimensions of the Si pillars. The corresponding strain maps are shown in Figure 4b,e,h, where we plot the in-plane biaxial tensile strain $\epsilon = (a - a_{\text{eq}})/a_{\text{eq}}$ (where a and a_{eq} are the strained and equilibrium in-plane lattice constants, respectively) deduced from the center position q_z of the Ge (004) peak. A clear lateral strain modulation commensurate with the sample thickness variations is observed in each case, with the measured strain going through a well-defined minimum at the location of each Si pillar. Additional random strain variations are also observed in the NM regions between neighboring pillars, likely caused by defects in the Ge lattice, roughness at the Ge/PI interface, and/or non-uniform plastic strain induced in the PI film by the applied stress. In any case, the size of these variations is sufficiently small not to obscure the strain modulation induced by the pillar array.

In particular, the blue streaks away from the pillars observed in Figure 4h suggest the formation of strain-induced cracks at the largest measured pressure of 621 kPa. This behavior has been discussed in our prior study of mechanically stressed Ge NMs of uniform thickness by Raman and photoluminescence spectroscopy,¹² where it manifested itself in a partial saturation of the strain–pressure curve at similar high pressures. Importantly, in the same study, it was also shown that the maximum pressure that can be applied before the onset of such plastic deformation can be further increased using thinner NMs.

The strain gradients on the NM plane in the patterned samples are further illustrated by the line cuts of Figure 4c,f,i, taken along the red dashed lines shown in the adjacent strain maps. At the boundaries of each pillar, the measured strain varies between the larger value outside the pillar (i.e., in the uncoated NM region) and the smaller value under the pillar on a length scale Δx on the order of 1 μm . The strain difference between uncoated and coated regions of the NMs is quantified in Table 1, where we list the average strain between the pillars

$\langle\epsilon_{\text{unc}}\rangle$, the minimum strain under the pillars ϵ_{min} , and their difference $\Delta\epsilon = \langle\epsilon_{\text{unc}}\rangle - \epsilon_{\text{min}}$ for all three data sets of Figure 4. For the NM regions between the pillars, we choose to quantify the strain with its spatial average (rather than the maximum value) because of the aforementioned random variations, which are described by the standard deviations also listed in the table. As expected, the strain difference $\Delta\epsilon$ increases with increasing gas pressure, illustrating the active tunability of these systems. Specifically, $\Delta\epsilon$ in Table 1 increases from about 0.2% at 255 kPa to 0.5% at 621 kPa. Additional measurements at multiple pressures will be required for a more detailed quantitative characterization of this dependence.

The resulting strain-induced lateral heterostructures in the Ge NMs are shown in Figure 5a–c, where we plot the conduction and valence band edges versus lateral position, as derived from the strain profiles of Figure 4c,f,i, respectively. These figures include the energies of both the direct (Γ) and indirect (L) conduction-band minima and the light-hole (LH) valence-band maximum, computed from the measured strain values using deformation potential theory.⁶ A detailed description of this theoretical model as applied to Ge NMs and a list of the relevant materials parameter values can be found in ref 13. For improved visual clarity, in Figure 5, we have omitted the inclusion of the heavy-hole (HH) valence band, which consistently lies at substantially lower energy (≥ 100 meV) compared to the LH band due to the strain-induced splitting illustrated in Figure 1b. The lateral variations in band edge energies observed in these plots are consistent with the discussion above [see Figure 1c]. Because of their lower biaxial tensile strain, the NM regions immediately underneath the a-Si pillars feature higher conduction-band minima and lower valence-band maxima and therefore act as potential-energy barriers for both types of carriers. The maximum barrier heights (i.e., band offsets) obtained at the highest applied pressure are on the order of 50, 15, and 35 meV for the Γ -valley electrons, L-valley electrons, and light holes, respectively. Furthermore, the energy separation between the direct and indirect conduction-band minima $E_{\text{CT}} - E_{\text{CL}}$ also exhibits significant spatial variations commensurate with the pillar array. As a result, a strong modulation in the density of both Γ electrons and light holes can be produced, with both types of carriers predominantly confined in the uncovered NM regions. From a technological standpoint, this behavior is particularly attractive for applications to light-emitting devices, where the controlled spatial confinement of carriers across the direct bandgap can be exploited to enhance key device parameters such as radiative recombination rate and optical gain.

The measured strain distributions were also modeled numerically with finite element simulations using COMSOL Multiphysics with the Solid Mechanics interface. In these simulations, we consider an array-coated Ge NM [Figure 6a] supported by a PI film with fixed lateral boundaries and uniform pressure applied in the upward direction (see Methods Section). The calculated strain profiles corresponding to the data of Figure 4c,f,i are shown in Figure 6b–d, respectively. The ability of the a-Si pillars to limit the strain in the underlying NM regions is well-reproduced in these simulation results. The quantitative agreement with the data of Figure 4 is also quite reasonable. The calculated strain difference $\Delta\epsilon$ between the regions in between and under the pillars increases with increasing pressure from about 0.3% in Figure 6b to 0.6% in Figure 6d, versus 0.2 to 0.5% in the

Table 1. Measured Strain Values from the Three Data Sets of Figure 4^a

sample	pressure (kPa)	ϵ_{unc} (%)	ϵ_{min} (%)	$\Delta\epsilon$ (%)
B	255	1.05 ± 0.02	0.85	0.20
A	414	1.53 ± 0.06	1.16	0.37
A	621	1.69 ± 0.11	1.20	0.49

^a ϵ_{unc} : Strain in the uncoated NM regions, expressed in terms of its average $\langle\epsilon_{\text{unc}}\rangle$ and standard deviation. Here, $\langle\epsilon_{\text{unc}}\rangle$ is computed by removing all data points under the pillar(s) (specifically, all data points where the strain falls below 45% of the maximum value in the map) and then averaging the strain measured at all other positions. ϵ_{min} : Minimum strain under the pillars. $\Delta\epsilon$: Strain difference $\langle\epsilon_{\text{unc}}\rangle - \epsilon_{\text{min}}$.

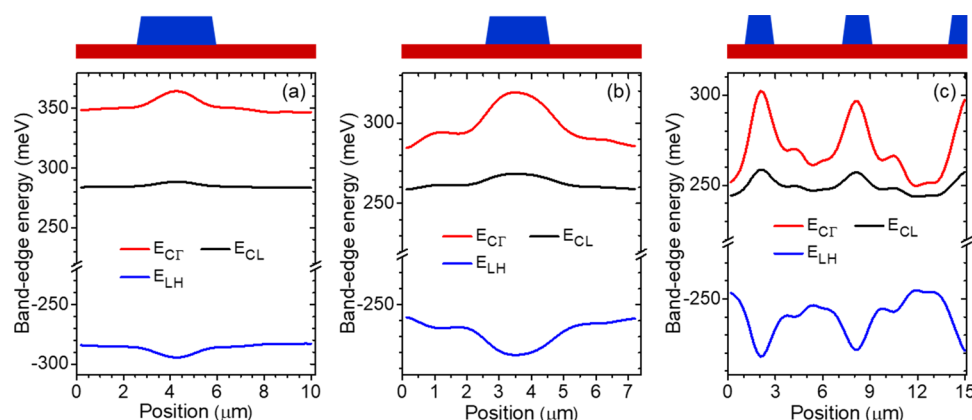


Figure 5. Strain-induced lateral heterostructures. (a–c) Conduction band lineup (band edge energy vs lateral position) at the Γ point (red traces) and in the L valleys (black traces) and light-hole valence-band lineup (blue traces) computed from the strain profiles of Figure 4c,f,i, respectively. The schematic cross-sectional images shown on top of each plot illustrate the positions and dimensions of the a-Si pillars (blue regions) on the Ge NMs (red regions). The fundamental bandgap energy is the difference between the black and blue traces. The direct bandgap energy is the difference between the red and blue traces. In panel (c), the red trace nearly crosses below the black one in the regions between the pillars [especially at a lateral position of $\sim 12 \mu\text{m}$, where the biaxial tensile strain is over 1.8%, as shown in Figure 4i], indicating that the Ge crystal is nearly a direct-bandgap material in these regions.

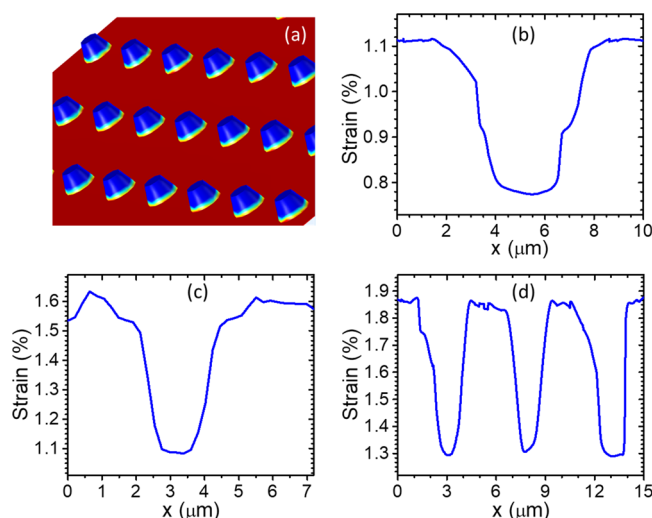


Figure 6. Finite-element strain simulation results. (a) Simulated sample geometry. The colors in this figure reflect the calculated strain distribution on the upper surface of the Ge NM and a-Si pillars. (b–d) Calculated Ge strain profiles along a line crossing through the center of one or multiple pillars, for the geometrical parameters and straining conditions of the experimental samples of Figure 4c,f,i, respectively.

measured strain maps (see Table 1). The strain gradients $\Delta\epsilon/\Delta x$ at the pillar boundaries are also somewhat larger in the simulated profiles compared to the experimental ones. These discrepancies may be attributed to deviations of the geometrical and materials parameters of the actual samples from the values used in the simulations, as well as meshing and discretization inaccuracies (which are also likely responsible for the fluctuations observed in the calculated strain profiles). It should also be noted that the SEM images of Figure 2a suggest incomplete adhesion of the deposited a-Si on the Ge surface around the rims of the pillars. This observation, together with possible variations in the slope of the pillar sidewalls, may explain the lower strain gradients observed in the experimental maps.

The maximum strain difference $\Delta\epsilon$ obtained with the samples under study is limited by the thickness ratio between the a-Si pillars and the Ge NM. To illustrate, in Figure 7a, we

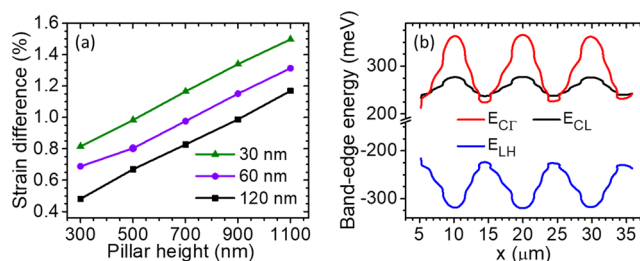


Figure 7. Geometrical tunability of the strain-induced band offsets. (a) Calculated strain difference $\Delta\epsilon$ between the regions in between and under the pillars plotted as a function of pillar height h for three values of NM thickness t . (b) Conduction-band lineup at the Γ point (red trace) and in the L valleys (black trace) and light-hole valence-band lineup (blue trace) computed from the simulated strain profile for $h = 1100 \text{ nm}$ and $t = 30 \text{ nm}$. All other geometrical parameter values used in these strain calculations are equal to those of sample B, and the induced stress in the NM is equivalent to an experimental applied pressure of 621 kPa.

plot the calculated values of $\Delta\epsilon$ for NMs of different thicknesses t (30, 60, and 120 nm) as a function of pillar height h between 300 and 1100 nm. All other geometrical parameters used in these simulations are the same as those of sample B, including a pillar base diameter of $D = 3.5 \mu\text{m}$, and the induced stress in the NM is equivalent to an experimental applied pressure of 621 kPa (the maximum value used in the measurements of Figure 4). As in Table 1, $\Delta\epsilon$ here is computed as the difference between the average strain between the pillars and the minimum strain under the pillars. A strain difference as large as 1.50% is obtained for the highest thickness ratio ($h = 1100 \text{ nm}$ and $t = 30 \text{ nm}$). The resulting conduction-band and valence-band lineups for $h = 1100 \text{ nm}$ and $t = 30 \text{ nm}$, computed from the simulated strain profiles, are plotted in Figure 7b. The band offsets in this plot are approximately 141, 40, and 96 meV for the Γ -valley electrons, L-valley electrons, and light holes, respectively, and a transition

from indirect- to direct-bandgap behavior is also observed in moving from under the pillars to the regions between them. These results therefore confirm the effectiveness of the present approach to develop pronounced strain-induced heterostructures with geometrically and actively tunable characteristics.

CONCLUSIONS

We have reported a new materials platform featuring controlled energy bandgap variations with position within a crystal of uniform chemical composition, based on the external application of stress in a film of variable thickness. The underlying lateral strain modulation has been mapped via XRD measurements, leveraging the unique combination of high spatial resolution and high strain sensitivity of the HXN beamline at NSLS-II. The specific samples investigated in this work consist of Ge NMs loaded with a periodic array of a-Si pillars, but similar results can be obtained with many other semiconductor materials and almost arbitrary distributions of strain-limiting elements patterned by nanolithography. In fact, strain-induced in-plane quantum confinement may also be envisioned in similar samples, through the formation of localized high-strain regions with lateral dimensions on the order of 10 nm (e.g., using a network of intersecting lines having such ultrasmall widths partially etched into a NM). The strain-induced heterostructures reported in this work are also promising for their significant long-term technological impact. In particular, a wide range of electronic and photonic devices would benefit from the ability to synthesize complex heterostructure lineups with multiple bandgap energies. Specific examples include multijunction solar cells and white LEDs, where multiple bandgaps would allow for efficient light absorption and emission, respectively, over a broad spectral range,⁶ and thermoelectric generators employing superlattice effects for enhanced conversion efficiency.³⁰ In their current form based on chemical heterostructures, however, these device concepts are limited by the choice of materials that can be grown on top of one another without excessive strain accumulation due to lattice mismatch. The use of strain to engineer variable energy bandgaps in uniform materials (e.g., using loading elements of different thicknesses on a strained NM) provides a promising new way to overcome these limitations. Active control of the bandgap energy by strain is also quite attractive as a way to provide dynamic reconfigurability and spectral tunability in optoelectronic devices such as diode lasers. Similarly, the ability to engineer energy-valley splittings through the introduction of anisotropic strain distributions may create novel application opportunities in spintronics and quantum computing. The same ideas could also be extended to future device technologies based on the emerging family of 2D crystals.⁴⁴ Finally, it should be noted that, while the gas-pressure-cell setup of Figure 2c is particularly convenient for basic experimental studies, similar straining effects can be obtained with piezoelectric actuators⁴⁵ or in integrated MEMS devices.⁴⁶ With the use of these techniques, combined with further advances in NM fabrication and thickness patterning, we can envision reaching the required level of control of the strain distribution for practical device applications.

METHODS

Fabrication. The Ge NMs are fabricated using commercial (Soitec) Ge-on-insulator (GOI) samples composed of a 90 nm-thick top (template) layer of Ge separated from a bulk Si substrate by a 150

nm-thick SiO₂ buried oxide layer (BOX). The Ge template layer is patterned and etched into an array of 1 × 1 mm² or 2 × 2 mm² mesas using standard photolithography and reactive-ion etching, exposing the underlying BOX around the mesa. Introduction of these structures into a 49% HF solution selectively etches the BOX, releasing the Ge mesas from the handle wafer. The samples are then placed in distilled deionized (DI) water where the Ge NMs float to the surface. The polyimide (PI-Kapton) substrates are prepared by spinning a layer of liquid PI onto commercial PI films. This process helps to smooth the PI surface and minimizes rippling in the Ge NMs after transfer. The liquid PI layer is cured by baking at 350 °C for 4 h under vacuum (2 Torr). The Ge NMs are typically collected from DI water by “scooping” them up with the PI substrate and allowing water to evaporate from the interface on a hot plate at 110 °C for around 30 min. The a-Si pillars are fabricated using electron beam lithography to pattern a square-periodic array of cylindrical holes in a PMMA resist previously spun on the NMs on PI. Amorphous Si is then deposited on the patterned PMMA by electron-beam evaporation followed by liftoff.

Measurements. The 2D strain profiles of Figure 4 were acquired by measuring the XRD intensity pattern around the Ge (004) peak with an X-ray nanobeam. The experiment was conducted at the HXN beamline of NSLS-II.^{25–28} In these measurements, an X-ray beam with 12 keV energy is focused on the NM surface with a spot size of about 40 nm using a Fresnel zone plate. The NM sample is tilted to the angle at which Bragg diffraction can be excited and collected. The diffraction pattern is recorded using a pixel-array detector (Merlin, Quantum Detectors) with 55 μm pixel size, located at a distance of about 35 cm away from the sample and oriented at an angle intercepting the diffracted beam perpendicularly. At the same time, the fluorescence signal is captured using an energy-dispersive detector (Vortex, Hitachi) placed at 90° with respect to the incident beam so that the Si pillars can be accurately mapped. Unlike conventional XRD measurements where the incidence angle is rocked while the position is fixed, here, we perform 2D raster scans at many angles across the Bragg peak. The scan step size in all the measurements of Figure 4 is between 150 and 200 nm, and at each position, a number of angles between 41 and 71 are measured in 0.05° intervals with a dwell time of 0.03 s. The combined 5D dataset (2D position on the NM, angle, and 2D pixel array detector) is aligned with the Si fluorescence map measured simultaneously so that the diffraction pattern can be obtained at each position. The center of mass of the XRD signal intensity versus out-of-plane wavenumber q_z (e.g., see Figure 3) is determined at each scanned position and used to derive the local out-of-plane strain ϵ_{\perp} based on the Bragg condition.⁴⁷ The in-plane strain ϵ is finally computed based on the assumption of plane stress condition, which is appropriate for our samples as discussed above. Under these conditions, in-plane and out-of-plane strain are simply related as $\epsilon_{\perp} = -2\sigma/(1 - \sigma)\epsilon = -2(C_{12}/C_{11})\epsilon$, where $\sigma = 0.28$ is the Ge Poisson ratio and $C_{11} = 128.53$ GPa and $C_{12} = 48.26$ GPa are the elastic stiffness constants.^{6,48} The use of bulk values for these material parameters in our NM samples is supported by the results of prior XRD studies with NMs of similar thickness.⁴⁹

Because a pixel-array detector is used to record the diffraction pattern where the angular spread is measured by pixels in real space, it is difficult to precisely determine the absolute angle without a reference sample measured under exactly the same conditions. As a result, this method is very accurate at determining relative strain variations across the sample area, but not the absolute strain. Consequently, in order to calibrate the experimental strain maps, we use the results of prior Raman measurements with similar unpatterned Ge NMs of the same thickness, strained with a similar pressure cell.¹² Specifically, the reference (zero strain) diffraction angle in the data analysis is selected so that, for each strain map, the average in-plane strain in the uncoated NM regions (ϵ_{unc}) matches the value measured in this Raman study at the same pressure (over micron-scale spot sizes). This calibration procedure relies on our prior observation that the strain–pressure relation in these Ge NMs is quite reproducible, with only small variations originating from residual strain at zero

pressure (on the order of 0.1% across different samples, including NMs coated with Si pillars).^{12,13,36}

Simulations. The COMSOL Multiphysics finite-element simulations of the NM strain distributions are based on a plane strain formulation where all out-of-plane stress components are assumed to be negligible.⁵⁰ Once again, this assumption is quite reasonable for the samples under study, where the applied pressure produces a spherical expansion of the NMs with very large radii of curvature relative to the NM thickness. The NM and PI thicknesses (90 nm and 125 μm , respectively) and all the geometrical parameters of the a-Si pillar arrays used in the simulations are equal to the measured or nominal values of the experimental samples, including a truncated conical shape with a 60° sidewall slope for the pillars. The relevant materials parameters for Ge, a-Si, and PI (i.e., Poisson ratio, Young's modulus, and density) are obtained from refs 48 and 51–54. For computational convenience, a square (rather than circular) geometry is used for the PI film and the overall simulation window, with fixed lateral boundaries and a physics-controlled triangular mesh. Uniform pressure is then applied in the upward direction. The simulated Ge NMs have a surface area of 130 $\mu\text{m} \times 130 \mu\text{m}$ and are located at the center of the supporting PI film. The size of the PI film is taken to be sufficiently large (50 mm \times 50 mm) to avoid any non-spherical deformation of the NM caused by edge effects near the fixed square boundaries of the PI film. Because of these geometrical differences between the experimental and simulated PI substrates, the values of the applied pressure that produce the same stress (and therefore strain) in the NM are also different. Therefore, we begin by modeling a Ge NM without any a-Si pillars and computing its strain–pressure relation in the simulated PI geometry. These results are then compared to the experimental strain–pressure relation measured in the aforementioned Raman study with an unpatterned Ge NM of the same thickness.¹² Based on this comparison, we finally determine the appropriate pressure values to use in the simulations of the three data sets of Figure 4.

AUTHOR INFORMATION

Corresponding Authors

Abdullah Gok – Department of Electrical and Computer Engineering and Photonics Center, Boston University, Boston, Massachusetts 02215, United States; Email: abdgok@bu.edu

Roberto Paiella – Department of Electrical and Computer Engineering and Photonics Center, Boston University, Boston, Massachusetts 02215, United States; orcid.org/0000-0002-7183-6249; Email: rpaiella@bu.edu

Authors

Xiaowei Wang – Department of Electrical and Computer Engineering and Photonics Center, Boston University, Boston, Massachusetts 02215, United States; orcid.org/0000-0002-0420-9659

Shelley Scott – Department of Materials Science and Engineering, University of Wisconsin – Madison, Madison, Wisconsin 53706, United States; orcid.org/0000-0002-1263-011X

Abhishek Bhat – Department of Materials Science and Engineering, University of Wisconsin – Madison, Madison, Wisconsin 53706, United States

Hanfei Yan – National Synchrotron Light Source II, Brookhaven National Laboratory, Upton, Upton, New York 11973, United States

Ajith Pattammattel – National Synchrotron Light Source II, Brookhaven National Laboratory, Upton, Upton, New York 11973, United States; orcid.org/0000-0002-5956-7808

Evgeny Nazaretski – National Synchrotron Light Source II, Brookhaven National Laboratory, Upton, Upton, New York 11973, United States; orcid.org/0000-0003-1207-8174

Yong S. Chu – National Synchrotron Light Source II, Brookhaven National Laboratory, Upton, Upton, New York 11973, United States

Zicong Huang – Department of Electrical Engineering, Columbia University, New York, New York 10027, United States

Richard M. Osgood, Jr – Department of Electrical and Computer Engineering and Photonics Center, Boston University, Boston, Massachusetts 02215, United States; Department of Electrical Engineering, Columbia University, New York, New York 10027, United States

Max G. Lagally – Department of Materials Science and Engineering, University of Wisconsin – Madison, Madison, Wisconsin 53706, United States

Complete contact information is available at:

<https://pubs.acs.org/10.1021/acsanm.1c00966>

Notes

The authors declare no competing financial interest.

ACKNOWLEDGMENTS

This work was supported in part by the U.S. Department of Energy (DOE), Office of Science, Basic Energy Sciences grant no. DE-FG02-03ER46028. The authors also acknowledge the use of facilities and instrumentation supported by NSF through the University of Wisconsin Materials Research Science and Engineering Center DMR-1121288. This research used the hard X-ray nanoprobe (HXN) beamline at 3-ID of the National Synchrotron Light Source II, a U.S. DOE Office of Science User Facility operated for the DOE Office of Science by Brookhaven National Laboratory under contract no. DE-SC0012704.

REFERENCES

- (1) Alferov, Z. I. Nobel Lecture: The Double Heterostructure Concept and Its Applications in Physics, Electronics, and Technology. *Rev. Mod. Phys.* **2001**, 73, 767–782.
- (2) Kroemer, H. Nobel Lecture: Quasielectric Fields and Band Offsets: Teaching Electrons New Tricks. *Rev. Mod. Phys.* **2001**, 73, 783–793.
- (3) Casey, H. C., Jr.; Panish, M. B. *Heterostructure Lasers, parts A and B*; Academic Press: Orlando, Florida, 1978.
- (4) Bir, G. L.; Pikus, G. E. *Symmetry and Strain-Induced Effects in Semiconductors*; Wiley: New York, 1974.
- (5) Chu, M.; Sun, Y.; Aghoram, U.; Thompson, S. E. Strain: A Solution for Higher Carrier Mobility in Nanoscale MOSFETs. *Annu. Rev. Mater. Res.* **2009**, 39, 203–229.
- (6) Chuang, S. L., *Physics of Photonic Devices*; Wiley: Hoboken, NJ, 2009.
- (7) Greil, J.; Lugstein, A.; Zeiner, C.; Strasser, G.; Bertagnolli, E. Tuning the Electro-Optical Properties of Germanium Nanowires by Tensile Strain. *Nano Lett.* **2012**, 12, 6230–6234.
- (8) Signorello, G.; Karg, S.; Björk, M. T.; Gotsmann, B.; Riel, H. Tuning the Light Emission from GaAs Nanowires over 290 meV with Uniaxial Strain. *Nano Lett.* **2013**, 13, 917–924.
- (9) Guilloy, K.; Pauc, N.; Gassenq, A.; Gentile, P.; Tardif, S.; Rieutord, F.; Calvo, V. Tensile Strained Germanium Nanowires Measured by Photocurrent Spectroscopy and X-Ray Microdiffraction. *Nano Lett.* **2015**, 15, 2429–2433.
- (10) Greil, J.; Assali, S.; Isono, Y.; Belabbes, A.; Bechstedt, F.; Valega Mackenzie, F. O.; Silov, A. Y.; Bakkers, E. P. A. M.; Haverkort, J. E.

M. Optical Properties of Strained Wurtzite Gallium Phosphide Nanowires. *Nano Lett.* **2016**, *16*, 3703–3709.

(11) Ding, F.; Singh, R.; Plumhof, J. D.; Zander, T.; Krápek, V.; Chen, Y. H.; Benyoucef, M.; Zwiller, V.; Dörr, K.; Bester, G.; Rastelli, A.; Schmidt, O. G. Tuning the Exciton Binding Energies in Single Self-Assembled InGaAs/GaAs Quantum Dots by Piezoelectric-Induced Biaxial Stress. *Phys. Rev. Lett.* **2010**, *104*, No. 067405.

(12) Sánchez-Pérez, J. R.; Boztug, C.; Chen, F.; Sudrajat, F. F.; Paskiewicz, D. M.; Jacobson, R. B.; Lagally, M. G.; Paiella, R. Direct-Bandgap Light-Emitting Germanium in Tensile Strained Nanomembranes. *Proc. Natl. Acad. Sci. U. S. A.* **2011**, *108*, 18893–18898.

(13) Boztug, C.; Sánchez-Pérez, J. R.; Cavallo, F.; Lagally, M. G.; Paiella, R. Strained-Germanium Nanostructures for Infrared Photonics. *ACS Nano* **2014**, *8*, 3136–3151.

(14) Martín-Sánchez, J.; Trotta, R.; Piredda, G.; Schimpf, C.; Trevisi, G.; Seravalli, L.; Frigeri, P.; Stroj, S.; Lettner, T.; Reindl, M.; Wildmann, J. S.; Edlinger, J.; Rastelli, A. Reversible Control of In-Plane Elastic Stress Tensor in Nanomembranes. *Adv. Opt. Mater.* **2016**, *4*, 682–687.

(15) Wang, X.; Cui, X.; Bhat, A.; Savage, D. E.; Reno, J. L.; Lagally, M. G.; Paiella, R. Ultrawide Strain-Tuning of Light Emission from InGaAs Nanomembranes. *Appl. Phys. Lett.* **2018**, *113*, 201105.

(16) de Kersauson, M.; El Kurdi, M.; David, S.; Checoury, X.; Fishman, G.; Sauvage, S.; Jakomin, R.; Beaudoin, G.; Sagnes, I.; Boucaud, P. Optical Gain in Single Tensile-Strained Germanium Photonic Wire. *Opt. Express* **2011**, *19*, 17925–17934.

(17) Nam, D.; Sukhdeo, D.; Roy, A.; Balram, K.; Cheng, S.-L.; Huang, K. C.-Y.; Yuan, Z.; Brongersma, M.; Nishi, Y.; Miller, D.; Saraswat, K. Strained Germanium Thin Film Membrane on Silicon Substrate for Optoelectronics. *Opt. Express* **2011**, *19*, 25866–25872.

(18) Minamisawa, R. A.; Süess, M. J.; Spolenak, R.; Faist, J.; David, C.; Gobrecht, J.; Bourdelle, K. K.; Sigg, H. Top-Down Fabricated Silicon Nanowires Under Tensile Elastic Strain up to 4.5%. *Nat. Commun.* **2012**, *3*, 1096.

(19) Millar, R. W.; Gallacher, K.; Samarelli, A.; Frigerio, J.; Chrastina, D.; Isella, G.; Dieing, T.; Paul, D. J. Extending the Emission Wavelength of Ge Nanopillars to 2.25 μm Using Silicon Nitride Stressors. *Opt. Express* **2015**, *23*, 18193–18202.

(20) Freund, L. B.; Suresh, S. *Thin Film Materials: Stress, Defect Formation and Surface Evolution*; Cambridge University Press: Cambridge, UK, 2003.

(21) Cavallo, F.; Grierson, D. S.; Turner, K. T.; Lagally, M. G. “Soft Si.” Effective Stiffness of Supported Crystalline Nanomembranes. *ACS Nano* **2011**, *5*, 5400–5407.

(22) Rogers, J. A.; Lagally, M. G.; Nuzzo, R. G. Synthesis, Assembly and Applications of Semiconductor Nanomembranes. *Nature* **2011**, *477*, 45–53.

(23) Guo, Q.; Di, Z.; Lagally, M. G.; Mei, Y. Strain Engineering and Mechanical Assembly of Silicon/Germanium Nanomembranes. *Mater. Sci. Eng. R* **2018**, *128*, 1–31.

(24) Liu, Z.; Wu, J.; Duan, W.; Lagally, M. G.; Liu, F. Electronic Phase Diagram of Single-Element Silicon “Strain” Superlattices. *Phys. Rev. Lett.* **2010**, *105*, No. 016802.

(25) Nazaretski, E.; Lauer, K.; Yan, H.; Bouet, N.; Zhou, J.; Conley, R.; Huang, X.; Xu, W.; Lu, M.; Gofron, K.; Kalbfleisch, S.; Wagner, U.; Rau, C.; Chu, Y. S. Pushing the Limits: An Instrument for Hard X-Ray Imaging below 20 nm. *J. Synchrotron Radiat.* **2015**, *22*, 336–341.

(26) Nazaretski, E.; Yan, H.; Lauer, K.; Bouet, N.; Huang, X.; Xu, W.; Zhou, J.; Shu, D.; Hwu, Y.; Chu, Y. S. Design and Performance of an X-ray Scanning Microscope at the Hard X-Ray Nanoprobe Beamline of NSLS-II. *J. Synchrotron Radiat.* **2017**, *24*, 1113–1119.

(27) Hill, M. O.; Calvo-Almazan, I.; Allain, M.; Holt, M. V.; Ulvestad, A.; Treu, J.; Koblmüller, G.; Huang, C.; Huang, X.; Yan, H.; Nazaretski, E.; Chu, Y. S.; Stephenson, G. B.; Chamard, V.; Lauhon, L. J.; Hruszkewycz, S. O. Measuring Three-Dimensional Strain and Structural Defects in a Single InGaAs Nanowire Using Coherent X-Ray Multiangle Bragg Projection Ptychography. *Nano Lett.* **2018**, *18*, 811–819.

(28) Cao, Y.; Assefa, T.; Banerjee, S.; Wieteska, A.; Wang, D. Z.-R.; Pasupathy, A.; Tong, X.; Liu, Y.; Lu, W.; Sun, Y.-P.; He, Y.; Huang, X.; Yan, H.; Chu, Y. S.; Billinge, S. J. L.; Robinson, I. K. Complete Strain Mapping of Nanosheets of Tantalum Disulfide. *ACS Appl. Mater. Interfaces* **2020**, *12*, 43173–43179.

(29) Kash, K.; der Gaag, B. P.; Mahoney, D. D.; Gozdz, A. S.; Florez, L. T.; Harbison, J. P.; Sturge, M. D. Observation of Quantum Confinement by Strain Gradients. *Phys. Rev. Lett.* **1991**, *67*, 1326–1329.

(30) Huang, M.; Ritz, C. S.; Novakovic, B.; Yu, D.; Zhang, Y.; Flack, F.; Savage, D. E.; Evans, P. G.; Knezevic, I.; Liu, F.; Lagally, M. G. Mechano-Electronic Superlattices in Silicon Nanoribbons. *ACS Nano* **2009**, *3*, 721–727.

(31) Nam, D.; Sukhdeo, D. S.; Kang, J.-H.; Petykiewicz, J.; Lee, J. H.; Jung, W. S.; Vučković, J.; Brongersma, M. L.; Saraswat, K. C. Strain-Induced Pseudoheterostructure Nanowires Confining Carriers at Room Temperature with Nanoscale-Tunable Band Profiles. *Nano Lett.* **2013**, *13*, 3118–3123.

(32) Bao, S.; Kim, D.; Onwukaeme, C.; Gupta, S.; Saraswat, K.; Lee, K. H.; Kim, Y.; Min, D.; Jung, Y.; Qiu, H.; Wang, H.; Fitzgerald, E. A.; Tan, C. S.; Nam, D. Low-Threshold Optically Pumped Lasing in Highly Strained Germanium Nanowires. *Nat. Commun.* **2017**, *8*, 1845.

(33) Armand Pilon, F. T.; Lyasota, A.; Niquet, Y.-M.; Reboud, V.; Calvo, V.; Pauc, N.; Widiez, J.; Bonzon, C.; Hartmann, J. M.; Chelnokov, A.; Faist, J.; Sigg, H. Lasing in Strained Germanium Microbridges. *Nat. Commun.* **2019**, *10*, 2724.

(34) Virgilio, M.; Grosso, G. Strain-Modulated Ge Superlattices. *J. Phys.: Condens. Matter* **2015**, *27*, 485305.

(35) Boztug, C.; Sánchez-Pérez, J. R.; Yin, J.; Lagally, M. G.; Paiella, R. Grating-Coupled Mid-Infrared Light Emission from Tensilely Strained Germanium Nanomembranes. *Appl. Phys. Lett.* **2013**, *103*, 201114.

(36) Yin, J.; Cui, X.; Wang, X.; Sookchoo, P.; Lagally, M. G.; Paiella, R. Flexible Nanomembrane Photonic-Crystal Cavities for Tensilely Strained-Germanium Light Emission. *Appl. Phys. Lett.* **2016**, *108*, 241107.

(37) Winarski, R. P.; Holt, M. V.; Rose, V.; Fuesz, P.; Carbaugh, D.; Benson, C.; Shu, D.; Kline, D.; Stephenson, G. B.; McNulty, I.; Maser, J. A Hard X-Ray Nanoprobe Beamline for Nanoscale Microscopy. *J. Synchrotron Radiat.* **2012**, *19*, 1056–1060.

(38) Hanke, M.; Dubslaff, M.; Schmidbauer, M.; Boeck, T.; Schöder, S.; Burghammer, M.; Riekel, C.; Patommel, J.; Schroer, C. G. Scanning X-Ray Diffraction with 200nm Spatial Resolution. *Appl. Phys. Lett.* **2008**, *92*, 193109.

(39) Chrastina, D.; Vanacore, G. M.; Bollani, M.; Boye, P.; Schöder, S.; Burghammer, M.; Sordan, R.; Isella, G.; Zani, M.; Tagliaferri, A. Patterning-Induced Strain Relief in Single Lithographic SiGe Nanostructures Studied by Nanobeam X-Ray Diffraction. *Nanotechnology* **2012**, *23*, 155702.

(40) Murray, C. E.; Ying, A.; Polvino, S. M.; Noyan, I. C.; Holt, M.; Maser, J. Nanoscale Silicon-on-Insulator Deformation Induced by Stressed Liner Structures. *J. Appl. Phys.* **2011**, *109*, No. 083543.

(41) Hrauda, N.; Zhang, J.; Wintersberger, E.; Etzelstorfer, T.; Mandl, B.; Stangl, J.; Carbone, D.; Holý, V.; Jovanović, V.; Biasotto, C.; Nanver, L. K.; Moers, J.; Grützmacher, D.; Bauer, G. X-Ray Nanodiffraction on a Single SiGe Quantum Dot Inside a Functioning Field-Effect Transistor. *Nano Lett.* **2011**, *11*, 2875–2880.

(42) Etzelstorfer, T.; Süess, M. J.; Schiefler, G. L.; Jacques, V. L. R.; Carbone, D.; Chrastina, D.; Isella, G.; Spolenak, R.; Stangl, J.; Sigg, H.; Diaz, A. Scanning X-Ray Strain Microscopy of Inhomogeneously Strained Ge Micro-Bridges. *J. Synchrotron Radiat.* **2014**, *21*, 111–118.

(43) Rhead, S. D.; Halpin, J. E.; Shah, V. A.; Myronov, M.; Patchett, D. H.; Allred, P. S.; Kachkanov, V.; Dolbnya, I. P.; Reparaz, J. S.; Wilson, N. R.; Sotomayor Torres, C. M.; Leadley, D. R. Tensile Strain Mapping in Flat Germanium Membranes. *Appl. Phys. Lett.* **2014**, *104*, 172107.

(44) Feng, J.; Qian, X.; Huang, C.-W.; Li, J. Strain-Engineered Artificial Atom as a Broad-Spectrum Solar Energy Funnel. *Nat. Photonics* **2012**, *6*, 866–872.

- (45) Martín-Sánchez, J.; Trotta, R.; Mariscal, A.; Serna, R.; Piredda, G.; Stroj, S.; Edlinger, J.; Schimpf, C.; Aberl, J.; Lettner, T.; Wildmann, J.; Huang, H.; Yuan, X.; Ziss, D.; Stangl, J.; Rastelli, A. Strain-Tuning of the Optical Properties of Semiconductor Nanomaterials by Integration onto Piezoelectric Actuators. *Semicond. Sci. Technol.* **2017**, *33*, 13001.
- (46) Christopher, J. W.; Vutukuru, M.; Lloyd, D.; Bunch, J. S.; Goldberg, B. B.; Bishop, D. J.; Swan, A. K. Monolayer MoS₂ Strained to 1.3% With a Microelectromechanical System. *J. Microelectromech. Syst.* **2019**, *28*, 254–263.
- (47) Robinson, I. K.; Tweet, D. J. Surface X-Ray Diffraction. *Rep. Prog. Phys.* **1992**, *55*, 599–651.
- (48) Fischetti, M. V.; Laux, S. E. Band Structure, Deformation Potentials, and Carrier Mobility in Strained Si, Ge, and SiGe Alloys. *J. Appl. Phys.* **1996**, *80*, 2234–2252.
- (49) Paskiewicz, D. M.; Scott, S. A.; Savage, D. E.; Celler, G. K.; Lagally, M. G. Symmetry in Strain Engineering of Nanomembranes: Making New Strained Materials. *ACS Nano* **2011**, *5*, 5532–5542.
- (50) Logan, D. L. *A First Course in the Finite Element Method*; Cengage Learning: Platteville, WI, 2017; pp. 305–310.
- (51) Jiang, T.; Khabaz, F.; Marne, A.; Wu, C.; Gearba, R.; Bodepudi, R.; Bonnacaze, R. T.; Liechti, K. M.; Korgel, B. A. Mechanical Properties of Hydrogenated Amorphous Silicon (a-Si:H) Particles. *J. Appl. Phys.* **2019**, *126*, 204303.
- (52) Joannopoulos, J. D.; Lukovsky, G. *The Physics of Hydrogenated Amorphous Si I*; Springer-Verlag: Berlin, Heidelberg, 1984; pp. 137–141.
- (53) Arafa, M.; Fay, P.; Ismail, K.; Chu, J. O.; Meyerson, B. S.; Adesida, I. High Speed P-Type SiGe Modulation-Doped Field-Effect Transistors. *IEEE Electron Dev. Lett.* **1996**, *17*, 124–126.
- (54) Dupont Kapton Polyimide Film General Specification. www.dupont.com/kapton/general/H-38479-4.pdf (Accessed 05 June 2020).